Received: 15 September 2019 | Revised: 29 September 2019 | Accepted: 5 October 2019

DOI: 10.1002/inf2.12057

ORIGINAL ARTICLE

WILEY

Optimization of sodium hydroxide for securing high thermoelectric performance in polycrystalline $Sn_{1-x}Se$ via anisotropy and vacancy synergy

Xiao-Lei Shi[1] | **Wei-Di Liu**[2] | **Ang-Yin Wu**[2] | **Van T. Nguyen**[2] | **Han Gao**[2] | **Qiang Sun**[2] | **Raza Moshwan**[2] | **Jin Zou**[2,3] | **Zhi-Gang Chen**[1]

[1]Centre for Future Materials, University of Southern Queensland, Springfield Central, Queensland, Australia

[2]Materials Engineering, The University of Queensland, Brisbane, Queensland, Australia

[3]Centre for Microscopy and Microanalysis, The University of Queensland, Brisbane, Australia

Correspondence
Zhi-Gang Chen,Centre for Future Materials, University of Southern Queensland, Springfield Central, QLD 4300, Australia.
Email: zhigang.chen@usq.edu.au

Jin Zou, Materials Engineering and Centre for Microscopy and Microanalysis, The University of Queensland, Brisbane, QLD 4072, Australia.
Email: j.zou@uq.edu.au

Funding information
Australian Research Council

Abstract

The morphology and composition are two key factors to determine the thermoelectric performance of aqueously synthesized tin selenide (SnSe) crystals; however, their controlling is still under exploring. In this study, we report a high figure-of-merit (ZT) of ~1.5 at 823 K in p-type polycrystalline $Sn_{1-x}Se$ resulted from a synergy of morphology control and vacancy optimization, realized by carefully tuning the sodium hydroxide (NaOH) concentration during solvothermal synthesis. After a comprehensive investigation on various NaOH concentrations, it was found that an optimized NaOH amount of 10 mL with a concentration of 10 mol L^{-1} can simultaneously achieve a large average crystal size and a high Sn vacancy concentration of ~2.5%. The large microplate-like crystals lead to a considerable anisotropy in the sintered pellets, and the high Sn vacancy level contributes to an optimum hole concentration to the level of $\sim 2.3 \times 10^{19}$ cm^{-3}, and in turn a high power factor of ~7.4 μW cm^{-1} K^{-2} at 823 K, measured along the direction perpendicular to the sintering pressure. In addition, a low thermal conductivity of ~0.41 W m^{-1} K^{-1} is achieved by effective phonon scattering at localized crystal imperfections including lattice distortions, grain boundaries, and vacancy domains, as observed by detailed structural characterizations. Furthermore, a competitive compressive strength of ~52.1 MPa can be achieved along the direction of high thermoelectric performance, indicating a mechanically robust feature. This study provides a new avenue in achieving high thermoelectric performance in SnSe-based thermoelectric materials.

KEYWORDS

anisotropy, sodium hydroxide, thermoelectric, tin selenide, vacancy

1 | INTRODUCTION

Thermoelectric materials can directly convert heat to electricity by harvesting waste heat emitted in the environment, which provide a potential solution to relieve the stress of considerable energy shortage and environmental issues derived from the depletion of fossil fuels.[1-3] The dimensionless figure-of-merit ZT is defined to evaluate the efficiency of energy conversion for thermoelectric materials[4-6]:

$$ZT = \frac{S^2\sigma T}{\kappa}, \quad (1)$$

where σ is the electrical conductivity, S is the Seebeck coefficient, $S^2\sigma$ is the power factor, T is the absolute temperature, and κ is the thermal conductivity, which is composed of two parts, namely electronic thermal conductivity κ_e and lattice thermal conductivity κ_l, respectively.[7,8] It is of significance to achieve a high $S^2\sigma$ as well as a low κ to secure a high ZT. For σ, S, and κ_e, there are[2,9-11]:

$$\sigma = ne\mu, \quad (2)$$

$$S = \frac{8\pi^2 k_B^2}{3e\hbar^2} m^* T \left(\frac{\pi}{3n}\right)^{2/3}, \quad (3)$$

$$\kappa_e = L\sigma T, \quad (4)$$

where n is the carrier concentration (n for electrons in n-type semiconductor and p for holes in p-type semiconductor), e is the electrical charge, μ is the carrier mobility, k_B is the Boltzmann constant, $\hbar$ is the Planck constant, m^* is the carrier effective mass, and L is the Lorenz number, respectively. Considering that S, σ, and κ strongly couple with each other via tuning n or p, it is a considerable challenge to achieve a high ZT for thermoelectric materials.[12,13] Historically, to achieve a high electrical transport performance, strategies such as resonant state doping,[14] band convergence,[15] and quantum confinement,[16] were investigated to tune appropriate n or p.[17] Meanwhile, to reduce κ_l which is mostly determined by structure, structural designs including nanostructuring,[18] hierarchical architecturing,[19,20] and nanoprecipitate inducing,[21] were explored.

Among the up-to-date thermoelectric materials, tin selenide (SnSe) has attracted much attention due to its high-performance, low-toxic, and high-cost-effective features.[2,22-24] SnSe single crystals were reported to exhibit ultrahigh ZTs of ~2.6 at 923 K in p-type crystals[25] and ~2.8 at 773 K in n-type crystals,[26] owing to their noticeably low κ along specified crystal directions (the b-axis).[25,26] However, SnSe single crystals are difficult to be employed in thermoelectric devices due to their critical crystal growth techniques, prospective high cost for fabrications, and undesirable mechanical properties.[23,27] To solve this issue, polycrystalline SnSe becomes a good alternative.[2,28,29] Various methods have been explored to fabricate polycrystalline SnSe, such as melting (include arc melting),[30-32] mechanical alloying,[24] solid-state reaction,[33] and hydrothermal[34] or solvothermal syntheses.[35] Band engineering,[2,29,36] multiphase alloying,[2] and texturing[2,35] are three main strategies to improve the ZT of pristine SnSe, and significant progress has been made up to this day (the ZT was improved from ~0.5 to ~2.5 before 873 K).[30,37] However, it should be noticed that any heteroatoms by doping and/or secondary phases by alloying may seriously harm the mechanical properties of pristine SnSe,[2,5,38] which has been intentionally neglected in previous studies. In this situation, to achieve high ZTs in pure SnSe with acceptable mechanical properties is much significant and promising for applying to thermoelectric devices.[39]

In order to achieve high ZTs in pure polycrystalline SnSe, a key point is to tune an appropriate n or p, which can optimize the electrical transport properties[2,5] as discussed above. To achieve this goal, aqueous solution routes such as hydrothermal and solvothermal syntheses are good choices,[2] owing to their abilities to directly tune cation or anion vacancy concentrations under supercritical conditions, including high temperature and high vapor pressure of solvents.[2] As a typical case, a high ZT of ~1.36 was reported in p-type polycrystalline $Sn_{0.98}Se$ at 823 K, achieved by inducing ~2% Sn vacancies during solvothermal synthesis and in turn a high p of $\sim 1.5 \times 10^{19}$ cm^{-3} and a high $S^2\sigma$ of 6.95 μW cm^{-1} K^{-2}.[29] At the same time, through controlling the synthesis time, large $Sn_{0.98}Se$ microplates with an average size of ~100 μm can be achieved, which significantly strengthen the anisotropy of sintered pellets and in turn secure a high electrical transport performance along specific direction (perpendicular to the sintering pressure).[29] However, it should be noted that synthesis duration is not the only one controllable parameter during synthesis, and whether the tuning of other synthesis conditions, such as stoichiometric ratio and amount of precursors, solvent type, and synthesis temperature, can achieve the same goal or even better thermoelectric performance is still unknown.[2,3,5,38] Considering the increasing demand of employing to thermoelectric device with both high thermoelectric performance and robust mechanical feature, it is urgent to exploring all potential factors to determine the vacancy concentration and the morphology of synthesized crystals (both size and type).

Acid or alkaline added into the aqueous synthesis plays significant roles in adjusting the pH of solutions and acting as precursors, both benefiting to the chemical reactions during synthesis.[28,29,36,40,41] However, there are still lack of comprehensive studies on the role of alkaline for aqueously synthesized SnSe thermoelectric materials, such as their influence on crystallization and composition. To fill this gap, we investigated the morphology, structure, composition, and thermoelectric performance of p-type SnSe crystals by carefully tuning the sodium hydroxide (NaOH) concentration during solvothermal synthesis, as illustrated in Figure 1A, and establish the interlinks between these features. After a systematic study based on various NaOH concentrations, we confirmed that an optimized NaOH amount of 10 mL with a high concentration of 10 mol L^{-1} can simultaneously achieve a large average crystal size and a high Sn vacancy concentration of

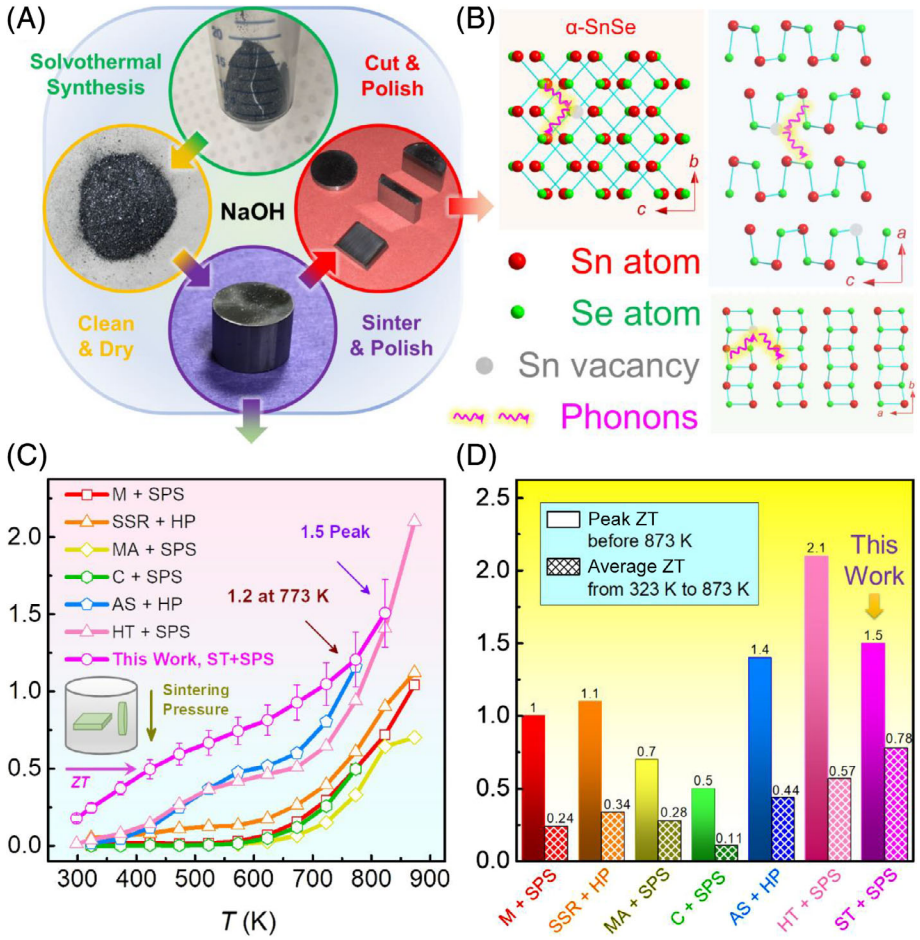

FIGURE 1 Illustrations of fabrication, structure, and thermoelectric performance of polycrystalline $Sn_{1-x}Se$. A, Schematic diagram of fabrication process; B, crystal structures viewed along different directions (for α-SnSe); C, temperature-dependent *ZT*; D, peak and average *ZT*s of our polycrystalline $Sn_{1-x}Se$ along the direction perpendicular to the sintering pressure (⊥). Reported *ZT*s from pure polycrystalline SnSe fabricated by different synthesis routes are also provided in both C and D for comparisons.[31,32,39,42-44] AS,[43] aqueous solution; C,[39] combustion; HP,[31,43] hot pressing; HT,[44] hydrothermal; M,[32] melting; MA,[42] mechanical alloying; SPS,[32,39,42,44] sparkle plasma sintering; SSR,[31] solid-state reaction; ST, solvothermal

∼2.5%. The large crystals lead to a considerable anisotropy in the sintered pellets, and the high Sn vacancy level contributes to an optimum p of $\sim 2.3 \times 10^{19}$ cm^{-3} and in turn a high $S^2\sigma$ of ∼7.4 μW cm^{-1} K^{-2} at 823 K, measured along the direction perpendicular to the sintering pressure. Simultaneously, a low κ of ∼0.41 W m^{-1} K^{-1} is achieved by effective phonon scattering at localized crystal imperfections including lattice distortions, grain boundaries, and vacancies, as illustrated in Figure 1B, and confirmed by detailed structural characterizations, leading to a high ZT of ∼1.5 at 823 K. This value is very competitive compared with previous studies focusing on pure polycrystalline SnSe via different fabrication techniques,[31,32,39,42-44] as shown in Figure 1C. Figure 1D shows that the achieved average ZT of ∼0.78 is also a record for pure polycrystalline SnSe according to previous results.[31,32,39,42-44] Furthermore, a competitive compressive strength of ∼52.1 MPa was also achieved along the direction of high thermoelectric performance, indicating a mechanically robust feature. This study provides a new avenue in achieving high thermoelectric performance in SnSe-based thermoelectric materials.

2 | RESULTS AND DISCUSSION

To investigate the impact of NaOH concentrations on the synthesized products, X-ray diffraction (XRD) investigations were performed. Figure 2A shows the XRD patterns taken from synthesized products with different amounts of 10 mol L^{-1} NaOH during syntheses (from 0 to 12 mL), in a 2θ range from 20° to 70°. The peak intensities were normalized for better comparison. As can be clearly seen, when no NaOH was added into the synthesis (0 mL), all diffraction peaks can be indexed as the hexagonal structured $SnSe_2$ with lattice parameters of a = 0.381 and c = 0.614 nm and a space group of P $\bar{3}$ m1, according to the JCPDS 23-0602.

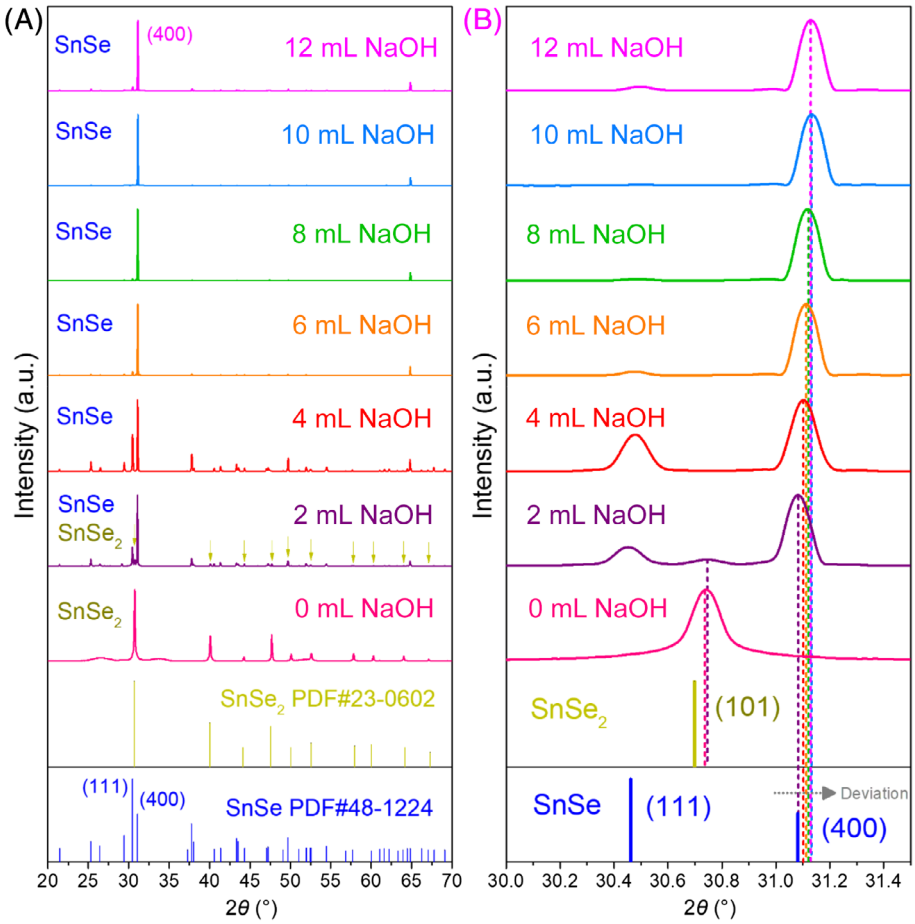

FIGURE 2 XRD results of synthesized products via different amounts of NaOH. A, XRD patterns in a 2θ range from 20° to 70°; B, magnified XRD patterns in a 2θ range from 30° to 31.5°. The peak intensities have been rescaled for better comparison. The concentrations of NaOH solutions used in the syntheses were all 10 mol L^{-1}. XRD, X-ray diffraction

When 2 mL NaOH was added into the synthesis, the diffraction peaks can be both indexed as hexagonal structured $SnSe_2$ (indexed by dark yellow arrows in Figure 2A), and orthorhombic-structured SnSe with lattice parameters of $a = 1.137$, $b = 0.419$, and $c = 0.444$ nm and a space group of Pnma, indicating the co-existence of SnSe and $SnSe_2$ phases. When 4 mL NaOH was added into the synthesis, all diffraction peaks can be indexed as orthorhombic structured SnSe. These results confirm that to secure pure SnSe phase, appropriate NaOH concentration is needed during syntheses (≥4 mL in this case, which should be adjusted when other synthesis parameters are changed such as precursor amount and solvent type).[2] As the 400* diffraction peak is the strongest peak, synthesized SnSe products must contain significant {100} surfaces, thus making the other peaks weak (such as 111* peaks),[28,41] showing similar feature of reported SnSe single crystals.[25,45,46]

To understand the reason why different phases are during a typical solvothermal synthesis, we note the following potential chemical reactions in the solution under high temperature and high vapor pressure[28,29,36,40,41]:

$$SnCl_2 \cdot 2H_2O \xrightarrow{C_2H_6O_2} Sn^{2+} + 2Cl^- + 2H_2O, \quad (5)$$

$$Na_2SeO_3 \xrightarrow{C_2H_6O_2} 2Na^+ + SeO_3^{2-}, \quad (6)$$

$$SeO_3^{2-} + C_2H_6O_2 \rightarrow Se + C_2H_2O_2 + H_2O + 2OH^-. \quad (7)$$

Based on above reactions, when sufficient NaOH is added into the solution, a high concentration of OH^- ions can benefit the ion reaction[35]:

$$3Se + 6OH^- \rightarrow 2Se^{2-} + SeO_3^{2-} + 3H_2O, \quad (8)$$

$$Sn^{2+} + Se^{2-} \rightarrow SnSe. \quad (9)$$

However, where NaOH is insufficient, Sn^{2+} can be oxidized by remained Se due to the fact that Se is more oxidative than Sn^{2+}[34,35]:

$$Se + Sn^{2+} \rightarrow Se^{2-} + Sn^{4+}, \quad (10)$$

$$Sn^{4+} + 2Se^{2-} \rightarrow SnSe_2. \quad (11)$$

Figure 2B shows the detailed XRD patterns in a 2θ range from 30° to 31.5°, in which, with increasing the NaOH amount from 4 to 10 mL, the peak intensities of 111* become weaker, indicating that the {100} surfaces of synthesized products become more significant,[29,40] implying a larger crystal size.[29,40,41] This is because SnSe has a typical layered structure,[2] the adjacent SnSe layers are mainly bound to each other along the *a*-axis with a combination of van der Waals forces,[47] making the crystals be difficult to grow along the *a*-axis due to the high surface energy,[2] thus the {100} surface is the most naked surface for the synthesized crystals. At the same time, with increasing the NaOH amount from 4 to 10 mL, the 400* peaks slightly shift toward right from standard $2\theta = 31.081°$, indicating a slightly reduced lattice parameter *a*,[29,36] and in turn a shrunken unit cell caused by the Sn vacancies in SnSe.[29] Furthermore, for the synthesized products via 12 mL NaOH, the position of the 400* peak has the same peak position of the products via 10 mL NaOH, indicating that both synthesized products have the same Sn vacancy level. On the other hand, the 111* peak intensity become much stronger in the products made by 12 mL NaOH, indicating a reduction in dimension of synthesized crystals. These results indicate that there is an upper limit for Sn vacancy concentration and an optimal crystal size when tuning the amount of NaOH, which can be explained by the situation that excessive ion concentration (both Na^+ and OH^-) may seriously inhibit the crystal growth of SnSe, which has also been found in other material systems.[48,49]

To verify the influence of different NaOH concentrations on the morphology and composition variations of synthesized products, comprehensive scanning electron microscopy (SEM), transmission electron microscopy (TEM), and energy dispersive spectroscopy (EDS) investigations were performed. For the synthesized pure $SnSe_2$ without NaOH addition, Figure 3A shows the typical optical image, from which dark yellow powders can be observed. Figure 3B shows corresponding SEM image with the inset of magnified SEM image, in which $SnSe_2$ powders with typical hexagonal morphologies can be seen. These powders occasionally agglomerate to form large-sized particles. Figure 3C shows a TEM image of a typical $SnSe_2$ microplate with the insets showing the corresponding selected area electron diffraction (SAED) pattern (top right) and high-resolution TEM (HRTEM) image (bottom right), both viewed along the [001] direction. These results confirm the crystal nature of hexagonal structured $SnSe_2$. EDS results including spots and maps also confirm the nature of $SnSe_2$, as shown in Figure S1. In comparison, for the synthesized products with both SnSe and $SnSe_2$ phases via 2 mL NaOH, Figure 3D shows the typical optical image, from which the color of powders becomes gray. Figure 3E shows the corresponding SEM image, from which both microrods and microplates can be found. Figure 3F shows a magnified SEM image taken from Figure 3E, in which coexistence of microrod-shaped SnSe and microplate-shaped $SnSe_2$ can be witnessed. For the synthesized pure SnSe made by adding 4 mL NaOH, Figure 3G also shows the typical optical image, from which metallic silver-colored powders can be observed. Figure 3H shows the corresponding SEM image, from which SnSe powders possess two typical morphologies, namely microrods and microplates. Our intensive EDS results on these different powders indicate that SnSe microrods are close to perfect crystals with a stoichiometric ratio of Sn:Se = 1:1, while SnSe microplates exhibit a slight off-stoichiometric ratio of Sn:Se = ~0.985:1, as shown in Figure S2. We anticipate that the Sn vacancy can result in crystal growth along specific directions.[2] Figure 3I shows a TEM image of one typical SnSe microplate with insets of corresponding SAED pattern (top right) and HRTEM image (bottom right), both viewed along the [100] direction. These results confirm the crystal nature of orthorhombic structured SnSe. Since {100} surface is the most significant surface in SnSe microplates, the TEM results explain why the 400* diffraction peaks are the strongest in XRD results.

As shown in Figure 2, even though the synthesized products were all pure SnSe when the amount of NaOH was ≥4 mL, these products are still different from either their peak intensities or peak shifts, indicating their morphological and compositional differences among these products. To clarify these, comprehensive SEM and EDS investigations were performed. Figure 4A–C shows SEM images of synthesized products when 6, 8, and 10 mL NaOH were added into the solutions, the corresponding optical images are also shown in the insets. Combined with Figure 3G,H, it is clearly seen that with increasing the NaOH amount from 4 to 10 mL, the crystal size of synthesized microplates is enlarged. Extensive EDS results indicate that the average off-stoichiometric ratios of Sn:Se were ~0.983:1, ~0.98:1, and ~0.975:1 for 6, 8, and 10 mL NaOH, respectively, as shown in Figure S3A,C, indicating that the higher the Sn vacancy concentration, the larger the crystal dimension. In addition, the amount of microrod is gradually decreased and finally disappear when the amount of NaOH reaches to 10 mL, indicating that OH^- ions in the solutions can benefit the crystal growth of SnSe toward a high off-stoichiometric ratio ($Sn_{1-x}Se$) with the morphology of crystals transferring from microrods to microplates.

Nevertheless, it should be noted that excessive NaOH may prohibit the crystal growth of SnSe microplates, owing to the excessive ion concentration in the solution during synthesis. Figure 4D shows the SEM image with inset of optical

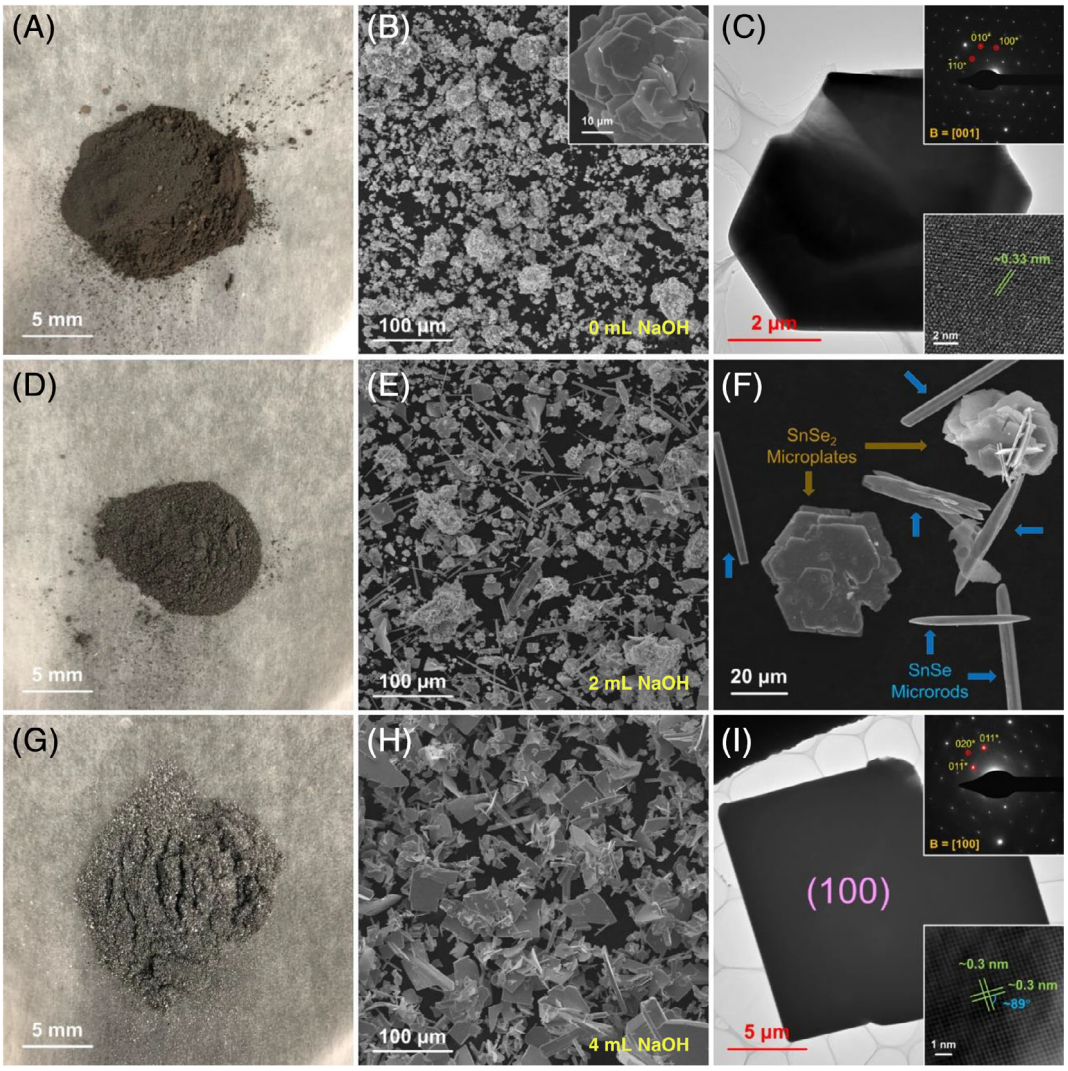

FIGURE 3 Morphological and structural characterizations of synthesized products via different amounts of NaOH. A, Optical image of synthesized products (pure $SnSe_2$) when no NaOH was added into the solution; B, corresponding SEM image with inset of magnified SEM image; C, corresponding TEM image with inset of SAED pattern (top right) and HRTEM image (bottom right) viewed along the [001] direction; D, optical image of synthesized products (SnSe and $SnSe_2$) when 2 mL NaOH was added into the solution, corresponding, E, low-magnification and, F, high-magnification SEM images; G, optical image of synthesized products (pure SnSe) when 4 mL NaOH was added into the solution; H, corresponding SEM image; I, corresponding TEM image with inset of SAED pattern (top right) and HRTEM image (bottom right) viewed along the [100] direction. The concentrations of NaOH solutions used in the syntheses were all 10 mol L^{-1}. HRTEM, high-resolution TEM; TEM, transmission electron microscopy; SAED, selected area electron diffraction; SEM, scanning electron microscopy

image of synthesized products made from 12 mL NaOH. Compared with Figure 4C, the crystal size becomes much smaller, even though the measured off-stoichiometric ratios of Sn:Se was ~0.975:1, same to the results from crystals via 10 mL NaOH as shown in Figure S3D, indicating that there is an upper limit for the Sn vacancy level when tuning the amount of NaOH, but excessive ion concentration should restrict the crystal growth.[48,49] Magnified SEM images of the microplates with much smaller size by 12 mL NaOH can be seen in Figure S3E,F. These dimension-reduced crystals also explain why the 111* peak of synthesized products via 12 mL NaOH becomes more significant than that of synthesized products via 10 mL NaOH.

To determine the thermoelectric performance of our synthesized SnSe crystals prepared with different NaOH concentrations, we sintered these crystals into polycrystalline pellets, cut these pellets long different directions, and fine-polished these samples for property measurements, as illustrated in Figure 1A. Before the measurements, detailed structural and compositional characterizations were performed on these pellets. Figure 5A shows the XRD patterns of pellets sintered from the synthesized SnSe crystals via both 10 and 12 mL NaOH, respectively, and the characterizations were taken along both the directions perpendicular (⊥) and parallel (//) to the sintering pressure. As can be seen, all diffraction peaks can be indexed as orthorhombic-structured SnSe,

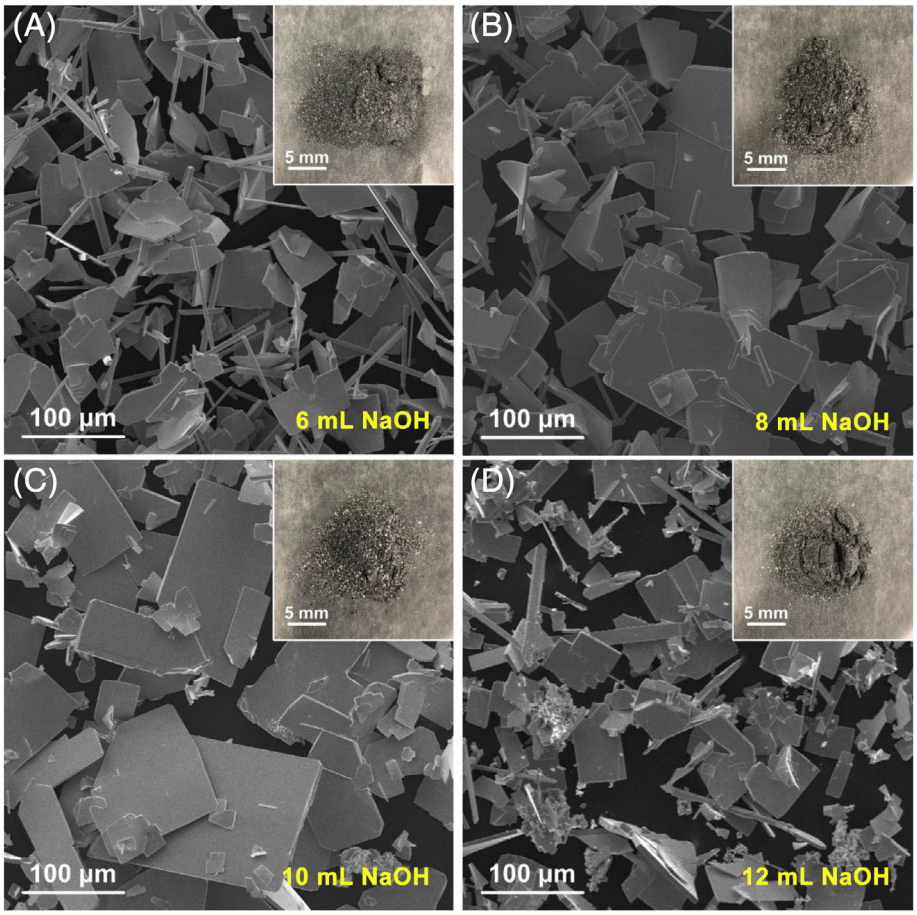

FIGURE 4 Morphological characterizations of synthesized products via different amounts of NaOH. SEM images with inset of optical images and average EDS results of synthesized products (pure SnSe) when, A, 6 mL NaOH, B, 8 mL NaOH, C, 10 mL NaOH, and, D, 12 mL NaOH were added into the solutions. The concentrations of NaOH solutions used in the syntheses were all 10 mol L^{-1}. EDS, energy dispersive spectroscopy; SEM, scanning electron microscopy

confirming the structural features maintained after the sintering.[28,36] Besides, for all samples, 400* peaks are the most significant along the ⊥ directions, while 111* peaks are strongest along the // directions, indicating considerable anisotropy in the pellets. Meanwhile, SnSe via 12 mL NaOH has a slightly stronger 111* peak than that via 10 mL NaOH along the ⊥ directions, indicating more significant anisotropy in pellets via 10 mL NaOH,[36] derived from their much larger grain sizes, agreeing with the XRD results of synthesized microplates shown in Figure 2. Figure 5B magnifies the 111* and 400* diffraction peaks to reveal the peak deviations, from which the same peak deviations of SnSe via 10 and 12 mL NaOH indicate same compositions, agreeing with the EDS results.

To clarify the anisotropy, composition, and structural features in sintered pellets, comprehensive SEM, EDS, electron probe microanalyzer (EPMA), and TEM investigations were performed. Figure 5C shows a SEM image with inset of optical image of cut and fine-polished pellets via 10 mL NaOH, from which a smooth surface without any obvious defect can be observed, indicating a good sintering quality. The measured densities ρ of these pellets were ~6.103, ~6.124, ~6.135, ~6.147, and ~6.122 g cm^{-3} for pellets by 4, 6, 8, 10, and 12 mL NaOH, respectively, indicating highly compact structures. Such high densities come from the large crystals (grains) composing the pellets, which is very close to the values of single crystals with a standard density of 6.179 g cm^{-3}.[45] Meanwhile, with increasing the NaOH concentration from 4 to 10 mL, the density is increased, mainly due to the larger size of synthesized microplates that lead to lower grain boundary density in the sintered pellets. Figure 5D,E shows SEM images of pellets via 10 mL NaOH, fractured from the ⊥ and the // directions, respectively. Highly textured structures can be observed, indicating a considerable anisotropy in the pellets, agreeing with the XRD results shown in Figure 5A,B. EPMA results indicate that the real stoichiometric ratios of Sn:Se in the sintered pellets were ~0.988:1, ~0.985:1, ~0.981:1, ~0.975:1, and ~0.975:1 for 4, 6, 8, 10, and 12 mL NaOH, respectively, as shown in Section 4 of Data S1. Figure 5F shows a HRTEM

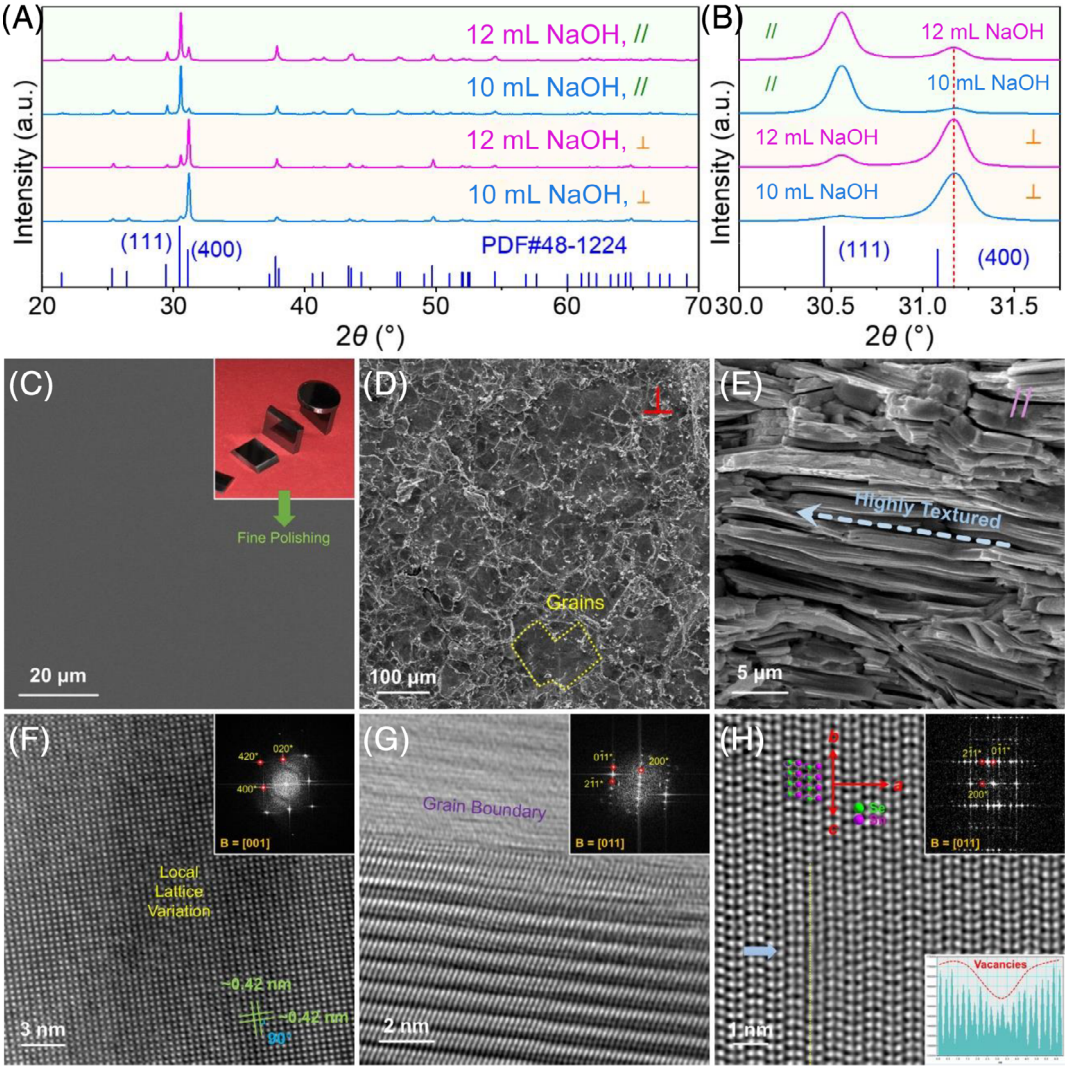

FIGURE 5 Morphological and structural characterizations of sintered pellets. A, XRD patterns of pellets via both 10 and 12 mL NaOH in a 2θ range from 20° to 70°, measured along different directions; B, magnified XRD patterns in a 2θ range from 30° to 31.75°; C, SEM image with inset of optical image of cut and fine-polished pellets (via 10 mL NaOH), SEM images of pellets fractured from, D, the ⊥ direction and, E, the // directions; F, HRTEM image with inset of FFT pattern viewed along the [001] direction to show local lattice variation[28,36,40]; G, HRTEM image with inset of FFT pattern viewed along the [011] direction to show a typical grain boundary[36]; H, high-resolution Cs-STEM HAADF image with inset of FFT pattern (top right) viewed along the [011] direction to show a vacancy domain revealed by the inset of line profile (bottom right).[40,44] The concentrations of NaOH solutions used in the syntheses were all 10 mol L^{-1}. FFT, fast Fourier transform; HRTEM, high-resolution TEM; SEM, scanning electron microscopy; XRD, X-ray diffraction

image taken from a pellet prepared with 10 mL NaOH with inset of fast Fourier transform (FFT) pattern viewed along the [001] direction. The results confirm the crystal nature of SnSe and show contrast variation, possibly due to inhomogeneous distrusted Sn vacancies.[28,36,40] Figure 5G shows a HRTEM image with inset of FFT pattern viewed along the [011] direction to show a typical grain boundary,[36] and Figure 5H shows a high-resolution Cs-STEM high-angle annular dark-field (HAADF) image viewed along the [011] direction to show a typical contrast variation, possibly due to the vacancies.[40,44] These results confirm the coexistence of various lattice imperfections in sintered pellets.

We measured thermoelectric properties from 300 to 823 K for SnSe pellets sintered from the crystals synthesized with different NaOH amounts from 4 to 12 mL (no the $SnSe_2$ phase), and the results are shown in Figure 6. High repeatability was confirmed by measuring the fluctuations being 10%, 2%, and 5% for σ, S, and κ, respectively, as shown in Figure S5. Besides, considering the anisotropy shown in Figure S6,[25,29] the ⊥ direction was chosen as the main direction for the property measurements.[41] Figure 6A shows the T-dependent σ of the pellets prepared from different amounts of NaOH. With increasing the NaOH amount from 4 to 10 mL, σ is gradually increased, benefitted from

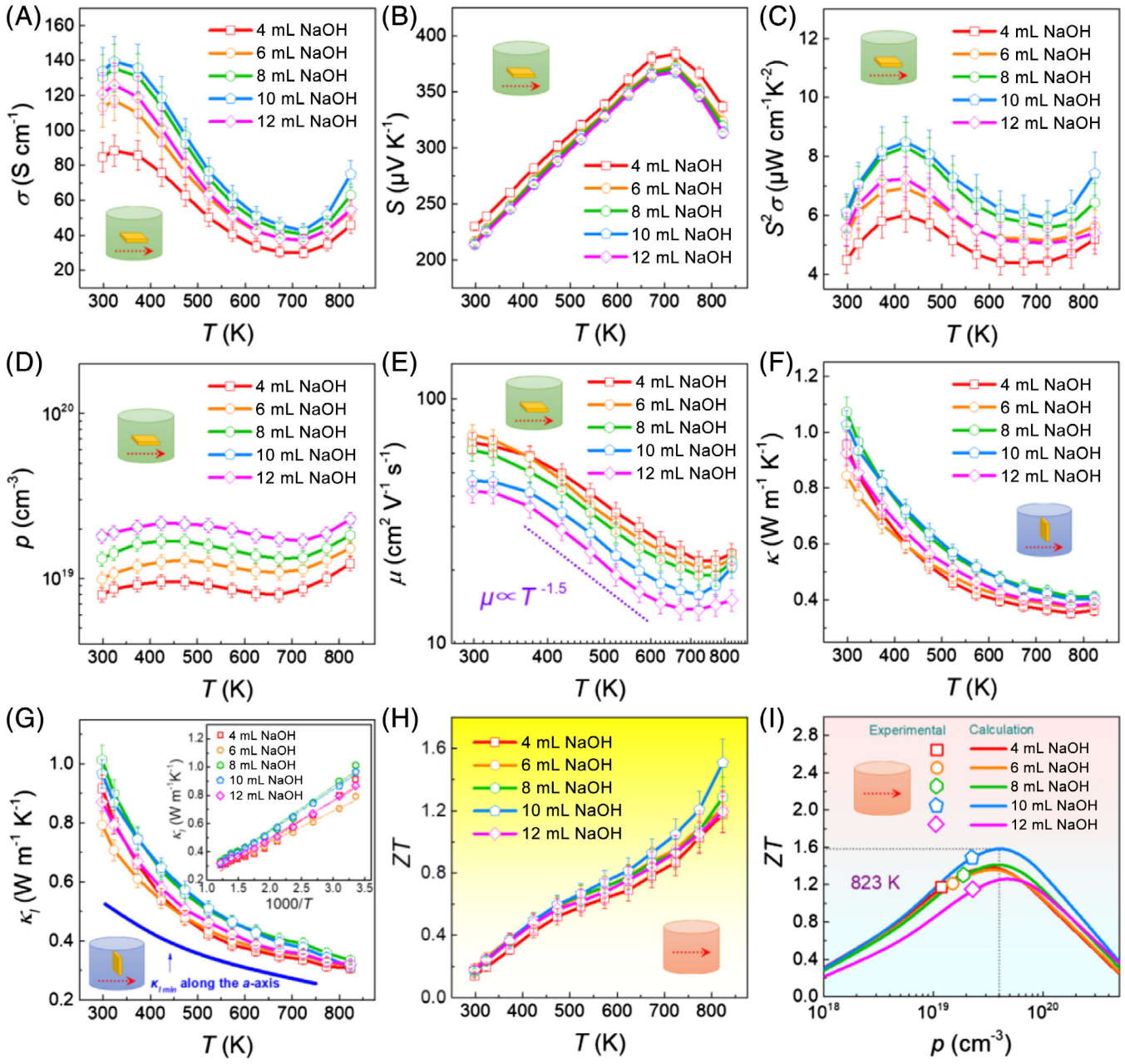

FIGURE 6 Plots of T-dependent properties from the pellets via different amounts of NaOH. A, σ; B, S; C, $S^2\sigma$; D, p; E, μ; F, κ; G, κ_l with inset of 1000/T-dependent κ_l; H, ZT; I, a comparison of achieved ZTs with calculated predicted ZTs at 823 K.[36,40,41,50] The concentrations of NaOH solutions used in the syntheses were all 10 mol L^{-1}

both the strengthened anisotropy and enhanced Sn vacancy concentration, which contributes to higher p. Compared with these pellets, σ of the pellet prepared from 12 mL NaOH drops, mainly derived from the reduction of anisotropy, as shown in Figure 5A,B. Figure 6B shows the T-dependent S of the pellets prepared from different amounts of NaOH. Oppositely, with increasing the NaOH amount from 4 to 10 mL, S decreases slightly, resulted from the enhanced Sn vacancy concentration. It is of interest to note that S of the pellets prepared from both 10 and 12 mL NaOH are almost the same, indicating that anisotropy has little influence on S.[2,29,41] Figure 6C shows the determined T-dependent $S^2\sigma$ of the pellets, in which a high $S^2\sigma$ of ~7.4 μW cm^{-1} K^{-2} at 823 K was achieved in the pellets prepared from 10 mL NaOH, benefited from both their considerable anisotropy and high Sn vacancy concentration. To determine p caused by the Sn vacancies, Figure 6D shows measured T-dependent p. With increasing the NaOH amount from 4 to 10 mL, p increases gradually, mainly coming from the extra holes provided by the enhanced Sn vacancy concentration. Figure 6E shows measured T-dependent μ. Different from σ, with increasing the NaOH amount from 4 to 10 mL, μ

decreases gradually, mainly owning to the enhanced vacancy concentration, which should cause lattice distortion, and in turn cause scatter the carriers during transportation. Note that μ of all pellets roughly follow the relationship of $\mu \propto T^{-1.5}$ in a wide temperature range from 350 to 750 K,[35] indicating that the scattering mechanism should still be dominated by acoustic phonon scattering.[35]

For the evaluation of thermal transport performance, Figure 6F shows the T-dependent κ of the pellets prepared from different amounts of NaOH. To determine κ using $\kappa = D\rho C_p$,[29,36] the measured D is shown in Figure S7A, and the specific heat capacity C_p was referred from our previous studies.[29,40,41] With increasing the NaOH amount from 4 to 10 mL, κ increases gradually, resulted from both the strengthened anisotropy and enhanced Sn vacancy concentration, which contributes to higher κ_e derived from higher σ according to Equations (4). Compared with the pellet prepared from 10 mL NaOH, κ of the pellet prepared from 12 mL NaOH was reduced, mainly derived from the anisotropy reduction, similar to σ. However, it should be noted that the higher Sn vacancy level should result in a strengthening of phonon scattering due to that Sn vacancies can be considered as point defects in the matrix, which can effectively scatter the phonons from mainly high frequencies.[2] Consequently, the understanding of both κ_e and κ_l is needed. To determine κ_e by Equation (4) and κ_l by $\kappa_l = \kappa - \kappa_e$, the calculated L is shown in Figure S7B by a classical single parabolic band (SPB) model, and the determined T-dependent κ_e is also shown in Figure S7C, which has similar trend of σ but much smaller values compared with κ. Figure 6G shows the T-dependent κ_l. Similar to κ, with increasing the NaOH amount from 4 to 10 mL, κ_l increases gradually, resulted from both the strengthened anisotropy and Sn vacancy concentration (strengthened point defects and local lattice distortions to effectively scatter the phonons). Compared with the pellet prepared from 10 mL NaOH, κ_l of the pellet prepared from 12 mL NaOH was also reduced, mainly derived from the anisotropy reduction, indicating that anisotropy also plays a significant role in determining the thermal transport properties in polycrystalline SnSe. The inset of Figure 6G shows determined 1000/T-dependent κ_l, which roughly following a linear relationship, showing that Umklapp phonon scattering dominates the phonon scattering mechanism in SnSe.[45] A low κ_l of only $\sim$0.31 W m^{-1} K^{-1} at 823 K was achieved from the pellet prepared from 10 mL NaOH, which was close to the calculated theoretical value of minimum κ_l ($\kappa_{l\,min}$) via a classical Debye-Cahill model,[51] from which the calculated $\kappa_{l\,min}$ were 0.26, 0.36, and 0.33 W m^{-1} K^{-1} along the a-axis, b-axis, and c-axis,[25] respectively. In fact, because this calculation is based on intrinsic SnSe single crystals with no defect and an ideal relative density of 100%, our achieved κ_l are reasonable lower than the calculated $\kappa_{l\,min}$. Such low κ_l are mainly derived from the anisotropy and crystal imperfections including Sn vacancy caused point defects/lattice distortions and grain boundaries (refer to Figure 5). These crystal imperfections can scatter phonons with different wavelengths, contributing to a low κ_l. Besides, the calculated T-dependent κ_l/κ ratio is shown in Figure S7D, from which more than $\sim$70% of κ were derived from the phonon transport (κ_l) when $T \leq 823$ K, indicating κ is dominated by phonon transport.

Figure 6H shows the determined T-dependent ZT. Surprisingly, a competitive ZT of $\sim$1.5 at 823 K was achieved from the pellets prepared from 10 mL NaOH, indicating that an appropriate NaOH amount in the synthesis can successfully realize a synergy of anisotropy strengthening by morphology controlling and carrier concentration improving. Figure 6I shows a comparison of experimental ZTs with predicted values by calculations based on the SPB model at 823 K,[52] in which our measured p value of $\sim 2.3 \times 10^{19}$ cm^{-3} is very close to the predicted value ($\sim 4 \times 10^{19}$ cm^{-3}) that corresponds a peak ZT of $\sim$1.6 for pure polycrystalline SnSe. Considering that our achieved $Sn_{1-x}Se$ has a maximum Sn vacancy concentration of $\sim$2.5%, tuning the vacancy concentration to an even higher level is a potential way to achieve higher p and ZT, and an appropriate design of synthesis route can achieve this goal, such as solvent and vapor pressure control. The density functional theory calculations of the electronic band structures of SnSe and $Sn_{1-x}Se$ in our previous studies confirmed that the Fermi level moves into the valence band with the presence of Sn vacancy in the supercell, indicating that the Sn vacancy changes SnSe into a degenerate p-type semiconductor with significantly increased p.[40,50] More discussions about the fundamental reasons of Sn vacancy concentration influencing on the electrical transport performance of SnSe can be referred to Figure S8. Except further improving the Sn vacancy level, there are several routes to further improve the p value to achieve even higher ZT. Considering that our achieved results are based on pure SnSe, doping with other elements such as Na and Ag which exhibit 1+ valence state can provide more holes in the system,[45,46] leading to higher p and ZT. Furthermore, alloying with other thermoelectric systems which have higher intrinsic p values such as Cu_2Se and SnTe is also a good choice.[3,53-56]

For the practical applications of our SnSe crystals, it is critical important to evaluate their mechanical properties. For this reason, we investigated the mechanical property for the SnSe pellet prepared from 10 mL NaOH using an Instron 5584 EM Frame machine, as shown in Figure 7A. The sintered pellets were cut into rectangular chips with 3.5 mm in width and thickness, and 7 mm in height. The entire surfaces of the specimens were finely polished to remove the scratches by cutting. Figure 7B shows the compressive strength values derived

from the extension-stress curves for the pellet (at a strain rate of 2.5×10^{-4} s^{-1}), from which competitive strength of ~52.1 and ~77.0 MPa can be achieved along the both ⊥ and // directions, respectively, both of which are very competitive with reported values of 74.4 MPa with a peak ZT of ~0.5 at 773 K.[39] This value is also comparable to the other commercial thermoelectric materials, such as PbTe and Bi_2Te_3.[57,58] Such an outstanding mechanical performance are mainly derived from the Sn vacancy-induced dispersion hardening for the grains,[59-61] which is similar to the strengthening mechanism of traditional metals and alloys.[59-61] Nevertheless, it should be noted that the compressive strength measured along the ⊥ direction is lower than that measured along the // direction, due to the fact that, along the ⊥ direction, the pellet is easier to crack along the textured grains due to the most significant {100} surfaces of SnSe crystals, as shown in the SEM image in Figure 7C; at the same time, the grains may also be easier to crack due to the weak van der Waals forces between adjacent SnSe layers,[47] as shown in the SEM image in Figure 7D. Eventually, the ZT of ~1.03 at 823 K was achieved along the // direction, as shown in Figure S6E, that is, competitive for thermoelectric devices. Note that along the // direction, the "slight crack" indicates that there was a slight crack happened in the sample during the compression test, but the sample kept almost stable and has not cracked into pieces, this is why the compression curve can continue to rise after the "slight crack" until the entire pellet cracked. Such a slight crack should be derived from the layered structure in the sintered pellets. In fact, according to the famous Hall-Petch relationship ($\delta = \delta_0 + \kappa g^{-1/2}$, where δ is the yield strength of polycrystalline materials, δ_0 is the yield strength of a single crystal, g is the average grain size, and K is a constant),[62] a higher mechanical property may be further achieved when reducing the grain size of SnSe pellets. However, such a grain refinement may reduce the anisotropy and in turn harm the thermoelectric performance of polycrystalline SnSe along specific directions. Therefore, a balance of thermoelectric and mechanical properties is need for securing a practical candidate.

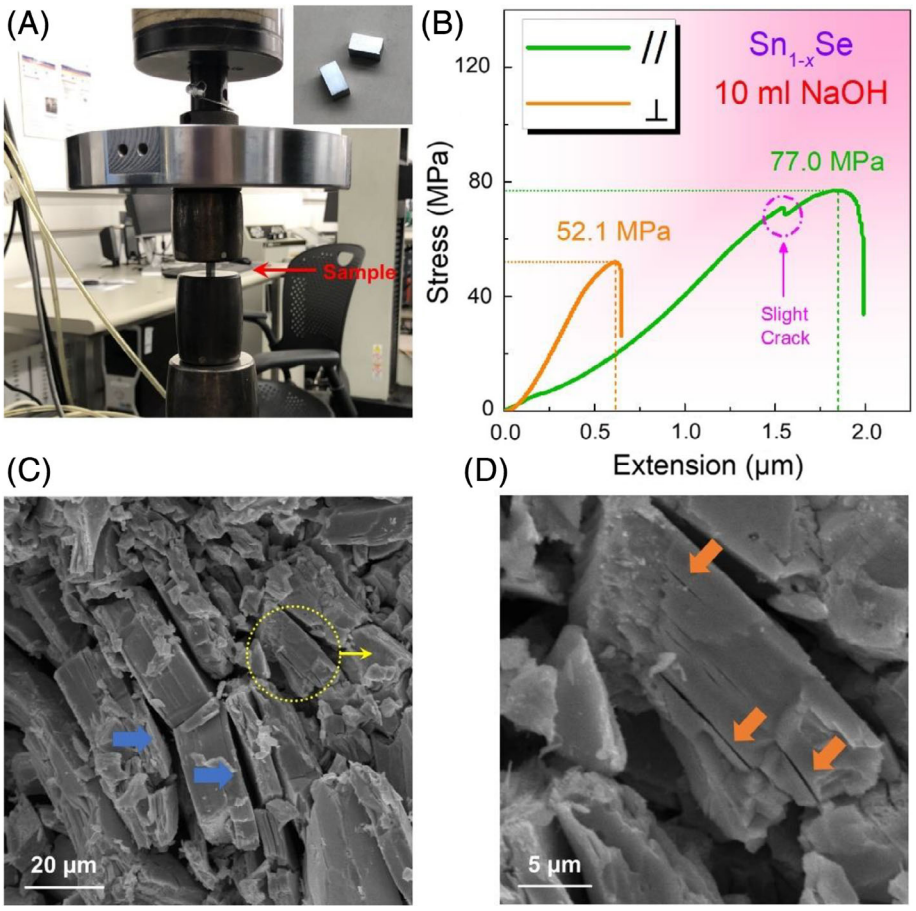

FIGURE 7 Mechanical properties with different measured directions for $Sn_{1-x}Se$ pellets via 10 mL NaOH: A, illustration of measurement; B, extension-dependent stress curves. The measured direction perpendicular to the sintering pressure is labelled as "⊥" and the measured direction parallel to the sintering pressure is labeled as "//"; C, SEM image of cracked samples to show the detached grains; D, SEM image of microcracks in the grains. SEM, scanning electron microscopy

3 | CONCLUSIONS

In this study, we demonstrate a synergy of morphology controlling and vacancy engineering to realize a high ZT of ~1.5 at 823 K and a competitive compressive strengthen of ~52.1 MPa in p-type polycrystalline $Sn_{1-x}Se$, achieved by carefully tuning the NaOH concentration during solvothermal synthesis. At the optimized NaOH amount of 10 mL with a high concentration of 10 mol L^{-1} can simultaneously enhance crystal dimensions and improve Sn vacancy concentration to ~2.5%, contributing to an optimum hole concentration of $\sim 2.3 \times 10^{19}$ cm^{-3} and in turn a high power factor of ~7.4 μW cm^{-1} K^{-2} at 823 K, measured along the direction perpendicular to the sintering pressure. Simultaneously, a low thermal conductivity of ~0.41 W m^{-1} K^{-1} is achieved by effective phonon scattering at localized crystal imperfections, securing a high ZT at this temperature. This study provides a new avenue in achieving high thermoelectric performance in SnSe-based thermoelectric materials.

4 | EXPERIMENTAL SECTION

4.1 | Synthesis

In this study, polycrystalline SnSe pellets were fabricated by a combination of solvothermal synthesis and sparkle plasma sintering (SPS) technique. For solvothermal synthesis, the Sn source was $SnCl_2{\cdot}2H_2O$ (99.99%), the Se source was Na_2SeO_3 (99.99%), the solvent was ethylene glycol (EG) anhydrous ($C_2H_6O_2$, 99.8%), and the alkaline was NaOH (99.99%). All chemicals were purchased from Sigma-Aldrich Co. LLC. To study the influence of NaOH concentrations on the morphology, structure, composition, and thermoelectric performance of synthesized SnSe, various NaOH amounts were investigated. In typical syntheses, for each autoclave, 0.01 mol Na_2SeO_3 and 0.01 mol $SnCl_2{\cdot}2H_2O$ were dissolved in EG (45 mL), and then added NaOH (10 mol L^{-1}) of 0, 2, 4, 6, 8, 10, and 12 mL for each autoclave, kept stirring for 15 minutes at room temperature. The solutions were then sealed in 125 mL polytetrafluoroethylene-lined stainless-steel autoclaves. These autoclaves were heated in an oven at 230°C for 48 hours, followed by naturally cooled to room temperature. The synthesized products were collected by centrifugation and washed by ethanol and deionized water for several times before drying in the oven at 60°C for 24 hours, as shown in Figure 1A. It should be noticed that to achieve a sintered pellet with an enough thickness for studying the anisotropy of properties, each pellet needs >6.0 g synthesized products (equal to four autoclaves) to achieve a thickness h of >7.0 mm. The dried products were sintered by SPS (SPS-211Lx, Fuji Electronic Co., Ltd) at 573°C for 5 minutes with a pressure of 70 MPa to form pellets with a dimension of Φ = 12.6 mm and h > 7.0 mm. The densities ρ of the sintered pellets were measured by the Archimedes method.[29] The sintered pellets were cut and fine-polished for measurements of thermoelectric performance, as shown in Figure 1A.

4.2 | Property

For measurements of thermoelectric properties, σ and S were simultaneously measured using an electric resistivity/Seebeck coefficient measuring system (ZEM-3, ULVAC Technologies, Inc.) in the temperature range between 300 and 823 K. The thermal diffusivity D was measured using the laser flash diffusivity method (LFA 457, NETZSCH Group). The κ was calculated as follows[25]:

$$\kappa = D\rho C_p, \tag{12}$$

where C_p is the specific heat capacity obtained by differential scanning calorimetry (DSC 404 C; NETZSCH Group), and the p was measured using the van der Pauw technique under a reversible magnetic field of 1.5 T. To ensure the repeatability thermoelectric properties, each pellet was measured for at least three times. For measurements of mechanical properties, the sintered pellets were cut into cuboidal chips of 3.5 mm in width and thickness, and 7 mm in length by diamond saw. All surfaces of the specimens were finely polished with 7000 mesh sandpapers to remove the scratches by cutting. Compressive strength measurements were carried out at a strain rate of 2.5×10^{-4} s^{-1} at room temperature (~25°C). A minimum of three specimens of each pellet were tested using an Instron 5584 EM Frame machine.

4.3 | Characterization

The XRD (Bruker-D8) was used to determine the crystal structures of both synthesized crystals and sintered pellets; the SEM (JSM-6610, JEOL Ltd.) with EDS, installed in JSM-6610 was used to study the morphology and composition of both synthesized crystals and sintered pellets; the TEM (TECNAI-F20) with installed EDS was used to study the morphology, structure, and composition of both synthesized crystals and sintered pellets; the Cs-STEM (Titan-G2) was used to study the structure of sintered pellets, the TEM specimens of sintered pellets were prepared by slicing the samples using focused ion beam technique (FEI Scios Dual-beam System); the EPMA (JEOL JXA-8200) was used to determine their compositions, the instrumental error of EMPA is 0.1%. There were 15 test areas for each sample.

4.4 | Calculation

A classical SPB model was used to calculate the L and p-dependent ZT for polycrystalline SnSe at a fixed temperature of 823 K. Calculation details are as follows[36,40,41,50]:

$$S(\eta)=\frac{k_B}{e}\bullet\left[\frac{(r+(5/2))\bullet F_{r+(3/2)}(\eta)}{(r+(3/2))\bullet F_{r+(1/2)}(\eta)}-\eta\right], \quad (13)$$

$$p=\frac{1}{e\bullet R_H}=\frac{(2m^*\bullet k_BT)^{3/2}}{3\pi^2\hbar^3}\bullet\frac{(r+(3/2))^2\bullet F^2_{r+(1/2)}(\eta)}{\left(2r+\frac{3}{2}\right)\bullet F_{2r+(1/2)}(\eta)}, \quad (14)$$

$$\mu=\left[\frac{e\pi\hbar^4}{\sqrt{2}(k_BT)^{3/2}}\frac{C_l}{E_{def}{}^2(m^*)^{5/2}}\right]\frac{(2r+(3/2))\bullet F_{2r+(1/2)}(\eta)}{(r+(3/2))^2\bullet F_{r+(1/2)}(\eta)}, \quad (15)$$

$$L=\left(\frac{k_B}{e}\right)^2\bullet\left\{\frac{(r+(7/2))\bullet F_{r+(5/2)}(\eta)}{(r+(3/2))\bullet F_{r+(1/2)}(\eta)}-\left[\frac{(r+(5/2))\bullet F_{r+(3/2)}(\eta)}{(r+(3/2))\bullet F_{r+(1/2)}(\eta)}\right]^2\right\}, \quad (16)$$

where η is the reduced Fermi level, k_B is the Boltzmann constant, r is the carrier scattering factor ($r=-1/2$ for acoustic phonon scattering), R_H is the Hall coefficient, C_l is the elastic constant for longitudinal vibrations, and E_{def} is the deformation potential coefficient, respectively. There is[36,40,41,50]

$$C_l=v_l^2\cdot\rho, \quad (17)$$

where v_l is the longitudinal sound velocity and taken as 2730 m s^{-1} in this study.[63] $F_i(\eta)$ is the Fermi integral, expressed as follows[36,40,41,50]:

$$F_i(\eta)=\int_0^\infty\frac{x^i}{1+e^{(x-\eta)}}dx, \quad (18)$$

ACKNOWLEDGMENTS

This work was financially supported by the Australian Research Council. The Australian Microscopy and Microanalysis Research Facility is acknowledged for providing characterization facilities.

ORCID

Zhi-Gang Chen https://orcid.org/0000-0002-9309-7993

REFERENCES

1. Zhu T, Liu Y, Fu C, Heremans JP, Snyder JG, Zhao X. Compromise and synergy in high-efficiency thermoelectric materials. *Adv Mater*. 2017;29:1605884.
2. Chen Z-G, Shi X, Zhao L-D, Zou J. High-performance SnSe thermoelectric materials: Progress and future challenge. *Prog Mater Sci*. 2018;97:283-346.
3. Moshwan R, Yang L, Zou J, Chen ZG. Eco-friendly SnTe thermoelectric materials: Progress and future challenge. *Adv Funct Mater*. 2017;27:1703278.
4. Chen R, Lee J, Lee W, Li D. Thermoelectrics of nanowires. *Chem Rev*. 2019;119:9260-9302.
5. Yang L, Chen Z-G, Dargusch MS, et al. High performance thermoelectric materials: Progress and their applications. *Adv Energy Mater*. 2017;8:1701797.
6. Tan G, Zhao LD, Kanatzidis MG. Rationally designing high-performance bulk thermoelectric materials. *Chem Rev*. 2016;116:12123-12149.
7. Hong M, Wang Y, Xu S, et al. Nanoscale pores plus precipitates rendering high-performance thermoelectric $SnTe_{1-x}Se_x$ with refined band structures. *Nano Energy*. 2019;60:1-7.
8. Zhao K, Qiu P, Shi X, Chen L. Recent advances in liquid-like thermoelectric materials. *Adv Funct Mater*. 2019;1903867. https://doi.org/10.1002/adfm.201903867.
9. Wang Y, Yang L, Shi X, et al. Flexible thermoelectric materials and generators: challenges and innovations. *Adv Mater*. 2019;31:1807916.
10. Xu S, Hong M, Shi X-L, et al. High-performance PEDOT: PSS flexible thermoelectric materials and their devices by triple post-treatments. *Chem Mater*. 2019;31:5238-5244.
11. Taloni A, Vodret M, Costantini G, Zapperi S. Size effects on the fracture of microscale and nanoscale materials. *Nat Rev Mater*. 2018;3:211-224.
12. He J, Tritt TM. Advances in thermoelectric materials research: looking back and moving forward. *Science*. 2017;357:9997.
13. Hong M, Zou J, Chen ZG. Thermoelectric GeTe with diverse degrees of freedom having secured superhigh performance. *Adv Mater*. 2019;31:1807071.
14. Heremans JP, Jovovic V, Toberer ES, et al. Enhancement of thermoelectric efficiency in PbTe by distortion of the electronic density of states. *Science*. 2008;321:554-557.
15. Pei Y, Shi X, LaLonde A, Wang H, Chen L, Snyder GJ. Convergence of electronic bands for high performance bulk thermoelectrics. *Nature*. 2011;473:66-69.
16. Tian Y, Sakr MR, Kinder JM, et al. One-dimensional quantum confinement effect modulated thermoelectric properties in InAs nanowires. *Nano Lett*. 2012;12:6492-6497.
17. Liu WD, Chen ZG, Zou J. Eco-friendly higher manganese silicide thermoelectric materials: Progress and future challenges. *Adv Energy Mater*. 2018;8:1800056.
18. Hong M, Chasapis TC, Chen Z-G, et al. n-type $Bi_2Te_{3-x}Se_x$ nanoplates with enhanced thermoelectric efficiency driven by wide-frequency phonon scatterings and synergistic carrier scatterings. *ACS Nano*. 2016;10:4719-4727.
19. Biswas K, He J, Blum ID, et al. High-performance bulk thermoelectrics with all-scale hierarchical architectures. *Nature*. 2012;489:414-418.
20. Zhou T, Wang L, Zheng S, et al. Self-assembled 3D flower-like hierarchical Ti-doped Cu_3SbSe_4 microspheres with ultralow thermal conductivity and high *zT*. *Nano Energy*. 2018;49:221-229.
21. Liu WS, Zhang Q, Lan Y, et al. Thermoelectric property studies on cu-doped n-type CuxBi2Te2. 7Se0. 3 nanocomposites. *Adv Energy Mater*. 2011;1:577-587.
22. Kutorasinski K, Wiendlocha B, Kaprzyk S, Tobola J. Electronic structure and thermoelectric properties of n- and p-type SnSe from first-principles calculations. *Phys Rev B*. 2015;91:205201.

23. Zhou Y, Zhao L-D. Promising thermoelectric bulk materials with 2D structures. *Adv Mater*. 2017;29:1702676.
24. Wei TR, Wu CF, Zhang X, et al. Thermoelectric transport properties of pristine and Na-doped $SnSe_{(1-x)}Te_{(x)}$ polycrystals. *Phys Chem Chem Phys*. 2015;17:30102-30109.
25. Zhao LD, Lo SH, Zhang Y, et al. Ultralow thermal conductivity and high thermoelectric figure of merit in SnSe crystals. *Nature*. 2014;508:373-377.
26. Chang C, Wu M, He D, et al. 3D charge and 2D phonon transports leading to high out-of-plane *ZT* in n-type SnSe crystals. *Science*. 2018;360:778-783.
27. Zhao L-D, Chang C, Tan G, Kanatzidis MG. SnSe: a remarkable new thermoelectric material. *Energ Environ Sci*. 2016;9:3044-3060.
28. Shi XL, Zheng K, Liu WD, et al. Realizing high thermoelectric performance in n-type highly distorted Sb-doped SnSe microplates via tuning high electron concentration and inducing intensive crystal defects. *Adv Energy Mater*. 2018;8:1800775.
29. Shi X, Chen Z, Liu W, et al. Achieving high figure of merit in p-type polycrystalline $Sn_{0.98}Se$ via self-doping and anisotropy-strengthening. *Energy Storage Mater*. 2018;10:130-138.
30. Sassi S, Candolfi C, Vaney JB, et al. Assessment of the thermoelectric performance of polycrystalline p-type SnSe. *Appl Phys Lett*. 2014;104:212105.
31. Popuri SR, Pollet M, Decourt R, Morrison FD, Bennett NS, Bos JWG. Large thermoelectric power factors and impact of texturing on the thermal conductivity in polycrystalline SnSe. *J Mater Chem C*. 2016;4:1685-1691.
32. Fu Y, Xu J, Liu G-Q, et al. Enhanced thermoelectric performance in p-type polycrystalline SnSe benefiting from texture modulation. *J Mater Chem C*. 2016;4:1201-1207.
33. Chen S, Cai K, Zhao W. The effect of Te doping on the electronic structure and thermoelectric properties of SnSe. *Phys B*. 2012;407:4154-4159.
34. Ge Z-H, Wei K, Lewis H, Martin J, Nolas GS. Bottom-up processing and low temperature transport properties of polycrystalline SnSe. *J Solid State Chem*. 2015;225:354-358.
35. Li Y, Li F, Dong J, et al. Enhanced mid-temperature thermoelectric performance of textured SnSe polycrystals made of solvothermally synthesized powders. *J Mater Chem C*. 2016;4:2047-2055.
36. Shi XL, Zheng K, Hong M, et al. Boosting the thermoelectric performance of p-type heavily Cu-doped polycrystalline SnSe via inducing intensive crystal imperfections and defect phonon scattering. *Chem Sci*. 2018;9:7376-7389.
37. Lee YK, Luo Z, Cho SP, Kanatzidis MG, Chung I. Surface oxide removal for polycrystalline SnSe reveals near-single-crystal thermoelectric performance. *Joule*. 2019;3:719-731.
38. Chen Z-G, Han G, Yang L, Cheng L, Zou J. Nanostructured thermoelectric materials: current research and future challenge. *Prog Nat Sci*. 2012;22:535-549.
39. Fu J, Su X, Xie H, et al. Understanding the combustion process for the synthesis of mechanically robust SnSe thermoelectrics. *Nano Energy*. 2018;44:53-62.
40. Shi X, Wu A, Feng T, et al. High thermoelectric performance in p-type polycrystalline cd-doped SnSe achieved by a combination of cation vacancies and localized lattice engineering. *Adv Energy Mater*. 2019;9:1803242.
41. Shi X, Wu A, Liu W, et al. Polycrystalline SnSe with extraordinary thermoelectric property via nanoporous design. *ACS Nano*. 2018;12:11417-11425.
42. Liu H, Zhang X, Li S, Zhou Z, Liu Y, Zhang J. Synthesis and thermoelectric properties of SnSe by mechanical alloying and spark plasma sintering method. *J Electron Mater*. 2017;46:2629-2633.
43. Li M, Liu Y, Zhang Y, et al. Crystallographically textured SnSe nanomaterials produced from the liquid phase sintering of nanocrystals. *Dalton Trans*. 2019;48:3641-3647.
44. Wei W, Chang C, Yang T, et al. Achieving high thermoelectric figure of merit in polycrystalline SnSe via introducing Sn vacancies. *J Am Chem Soc*. 2018;140:499-505.
45. Peng K, Lu X, Zhan H, et al. Broad temperature plateau for high *ZT*s in heavily doped p-type SnSe single crystals. *Energ Environ Sci*. 2016;9:454-460.
46. Zhao L-D, Tan G, Hao S, et al. Ultrahigh power factor and thermoelectric performance in hole-doped single-crystal SnSe. *Science*. 2016;351:141-144.
47. Erdemir A. Crystal chemistry and solid lubricating properties of the monochalcogenides gallium selenide and tin selenide. *Tribol Trans*. 2008;37:471-478.
48. Kondo M, Fukawa M, Guo L, et al. High rate growth of microcrystalline silicon at low temperatures. *J Non Cryst Solids*. 2000;266:84-89.
49. Xu Z, Xu L, Lai Q, Ji X. A PEG assisted sol-gel synthesis of $LiFePO_4$ as cathodic material for lithium ion cells. *Mater Res Bull*. 2007;42:883-891.
50. Jin M, Shi X-L, Feng T, et al. Super large $Sn_{1-x}Se$ single crystals with excellent thermoelectric performance. *ACS Appl Mater Interfaces*. 2019;11:8051-8059.
51. Cahill DG, Watson SK, Pohl RO. Lower limit to the thermal conductivity of disordered crystals. *Phys Rev B*. 1992;46:6131-6140.
52. Xu Y, Li W, Wang C, et al. Performance optimization and single parabolic band behavior of thermoelectric MnTe. *J Mater Chem A*. 2017;5:19143-19150.
53. Liu W, Shi X, Hong M, et al. Ag doping induced abnormal lattice thermal conductivity in Cu_2Se. *J Mater Chem C*. 2018;6:13225-13231.
54. Zhao L, Islam SMKN, Wang J, et al. Significant enhancement of figure-of-merit in carbon-reinforced Cu_2Se nanocrystalline solids. *Nano Energy*. 2017;41:164-171.
55. Moshwan R, Shi X-L, Liu W-D, et al. High thermoelectric performance in sintered octahedron-shaped Sn $(CdIn)_xTe_{1+2x}$ microcrystals. *ACS Appl Mater Interfaces*. 2018;10:38944-38952.
56. Moshwan R, Liu W-D, Shi X-L, Wang YP, Zou J, Chen ZG. Realizing high thermoelectric properties of SnTe via synergistic band engineering and structure engineering. *Nano Energy*. 2019;65:104056.
57. Zhao L-D, Zhang B-P, Li J-F, Zhou M, Liu WS, Liu J. Thermoelectric and mechanical properties of nano-SiC-dispersed Bi_2Te_3 fabricated by mechanical alloying and spark plasma sintering. *J Alloys Compd*. 2008;455:259-264.
58. Gelbstein Y, Gotesman G, Lishzinker Y, Dashevsky Z, Dariel MP. Mechanical properties of PbTe-based thermoelectric semiconductors. *Scr Mater*. 2008;58:251-254.

59. Hasemann G, Schneibel J, Krüger M, et al. Vacancy strengthening in Fe_3Al iron aluminides. *Intermetallics*. 2014;54:95-103.
60. Osetsky YN, Bacon DJ. Comparison of void strengthening in fcc and bcc metals: large-scale atomic-level modelling. *Mater Sci Eng A*. 2005;400:374-377.
61. Li Y-J, Hu Q-M, Xu D-S, Yang R. Strengthening of γ-TiAl-Nb by short-range ordering of point defects. *Intermetallics*. 2011;19:793-796.
62. Hansen N. Hall-Petch relation and boundary strengthening. *Script Mater*. 2004;51:801-806.
63. Xiao Y, Chang C, Pei Y, et al. Origin of low thermal conductivity in SnSe. *Phys Rev B*. 2016;94:125203.

SUPPORTING INFORMATION

Additional supporting information may be found online in the Supporting Information section at the end of this article.

How to cite this article: Shi X-L, Liu W-D, Wu A-Y, et al. Optimization of sodium hydroxide for securing high thermoelectric performance in polycrystalline $Sn_{1-x}Se$ via anisotropy and vacancy synergy. *InfoMat*. 2019;1–15. https://doi.org/10.1002/inf2.12057